JOURNAL OF APPLIED CRYSTALLOGRAPHY
ISSN 1600-5767

Microstructure and texture analysis of 304 austenitic stainless steel using Bragg edge transmission imaging

Mahdi Bakhtiari,[a] Fazlollah Sadeghi,[b]‡ Hirotaka Sato,[c] Wooyong Um,[a] Chang Hee Yim[b] and Hee-Seock Lee[a,d]*

[a]Division of Advanced Nuclear Engineering, Pohang University of Science and Technology, Pohang 37673, Republic of Korea, [b]Graduate Institute of Ferrous and Energy Materials Technology, Pohang University of Science and Technology, Pohang 37673, Republic of Korea, [c]Faculty of Engineering, Hokkaido University, Kita-13 Nishi-8, Kita-ku, Sapporo, Hokkaido 060-8628, Japan, and [d]Pohang Accelerator Laboratory, Pohang University of Science and Technology, Pohang 37673, Republic of Korea. *Correspondence e-mail: lee@postech.ac.kr

Received 25 April 2023
Accepted 27 July 2023

Edited by A. Borbély, Ecole National Supérieure des Mines, Saint-Etienne, France

‡ Present address: Brunel Centre for Advanced Solidification Technology (BCAST), Brunel University London, Uxbridge, Middlesex UB8 3PH, UK.

Keywords: neutron Bragg edge imaging; compact accelerator neutron sources; quantitative crystallographic analysis; microstructure; texture; 304 austenitic stainless steel; electron backscatter diffraction; non-destructive characterization; heat treatment.

Bragg edge imaging using pulsed neutrons is a non-destructive technique for studying microstructure and texture of materials. It provides two-dimensional visualization of crystallographic information using a pixelated gas electron multiplier detector and a time-of-flight method. In this work, the properties of type 304 austenitic stainless steel samples were studied via Bragg edge imaging. The samples included hot-rolled, cold-rolled and heat-treated specimens, which were characterized to investigate texture, phase fraction and grain growth. The results showed that the crystallite size increased with increasing annealing temperature. The cold-rolled and annealed samples exhibited strong textures, while the hot-rolled sample showed no preferred orientation. The phase volume fraction of induced martensite in the cold-rolled sample was also obtained. Two-dimensional maps of microstructures and textures were obtained without destructive processes. The results were validated by electron backscatter diffraction and found to be consistent. This work provides valuable information for non-destructive characterization of bulk materials by performing Bragg edge imaging using the Hokkaido University compact accelerator neutron source.

1. Introduction

Neutron Bragg edge imaging has shown promising abilities in studying the characteristics of structural materials such as steel. Bragg edge imaging reveals crystallographic information of bulk samples in two dimensions with reasonable spatial resolution (Vogel, 2000; Sato *et al.*, 2017; Su *et al.*, 2016). This technique has been used to study lattice strains (Ramadhan *et al.*, 2018); strain tomography (Hendriks *et al.*, 2019, 2017; Busi *et al.*, 2022); crystallite size, phase and texture (Sato *et al.*, 2011, 2021); and even lithium-ion batteries (Kamiyama *et al.*, 2017). Additionally, it can non-destructively analyze archeological and cultural artifacts (Shiota *et al.*, 2017; Cho *et al.*, 2021). Conventional methods such as electron backscatter diffraction (EBSD) (Sadeghi *et al.*, 2021), neutron and X-ray diffraction (Albertini *et al.*, 2000), and metallographic etching methods have been reliably used for material characterization. These methods are destructive and localized, and provide characteristics for material from a selected sample surface. In addition, the sample size must be small as these methods cannot obtain the material characteristics inside a bulk sample with a few centimetres dimension. Neutrons with deep penetration capability can obtain useful information from the

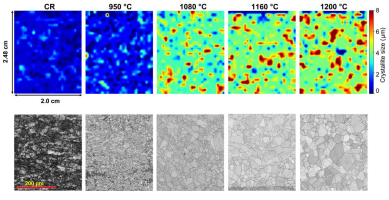

probed sample. Utilizing the neutron time of flight (TOF) and a pixelated detector with enough time and spatial resolution make Bragg edge imaging a powerful technique to gain a wealth of insight into the structure of materials (Sato *et al.*, 2018).

Bragg edge imaging is typically performed at pulsed spallation neutron sources such as ISIS 'IMAT' (Kockelmann *et al.*, 2018) and the Japan Proton Accelerator Research Complex (J-PARC) MLF BL22 'RADEN' (Shinohara *et al.*, 2020), where a neutron beam with high intensity and good wavelength resolution is achievable. However, beam time at these huge neutron sources is hard to access, and their construction is costly as well. In addition, the operation of such facilities needs many experienced operators. Compact accelerator neutron sources (CANSs), on the other hand, are becoming very useful in neutron applications such as Bragg edge imaging, due to their lower construction costs compared with large neutron source facilities and easier accessibility to their beam time. In recent years, CANS facilities have grown quite rapidly (Anderson *et al.*, 2016), including those based on photonuclear reactions (Bakhtiari *et al.*, 2022) using electron linacs (Kino *et al.*, 2019; Lu *et al.*, 2020). The experiment in this work, which has been conducted at a small-scale neutron source, shows the ability of CANSs in Bragg edge imaging. Developing a CANS is more straightforward than large neutron sources, with less cost, and they can be operated with trained students and staff. This helps with tackling limitation challenges of huge neutron sources and provides more available neutron beam time for the users.

In previous work (Bakhtiari *et al.*, 2023), we presented a conceptual design of a neutron source for Bragg edge imaging based on an electron linac as a CANS. Our planned facility is similar to the Hokkaido University Neutron Source (HUNS) in Japan (Furusaka *et al.*, 2014; Sato *et al.*, 2018). HUNS is a compact neutron source and is based on electron linacs, which makes it an ideal case for our neutron source development.

It was important to perform the experiment on samples of relevance from industrial and engineering points of view. Austenitic stainless steels have a variety of applications and have been the target of many studies up to now in the form of thin sheets. They are mainly produced via continuous casting, reheating, hot-rolling, cold-rolling and annealing processes (Sadeghi, 2022; Donadille *et al.*, 1989; Hedayati *et al.*, 2010; Huang *et al.*, 2012; Kheiri *et al.*, 2019; Tanhaei *et al.*, 2018; Hao *et al.*, 2020). Raabe (1997) showed that a hot-rolled (HR) structure presents a random texture, whereas a cold-rolled (CR) sample presents a brass texture. Chowdhury *et al.* (2005) observed Cu-type and Goss texture during cold rolling of austenitic stainless steel. The annealing process, on the other hand, has been shown to result in austenite reversion and nucleation of defect-free equi-axed grains (Sun *et al.*, 2015, 2018; Naghizadeh & Mirzadeh, 2016). Padilha *et al.* (2003) concluded that the microstructural outcome of the material depends on the rolling and annealing processes. We selected type 304 austenitic stainless steel samples for the measurement. Analysis of texture evolution and crystallite size via Bragg edge imaging helps us to improve engineering of advanced structural materials that require high strength and superior mechanical properties.

This work primarily aims to provide microstructure and texture analysis of the type 304 austenitic stainless steel samples using neutron Bragg edge imaging. This characterization is critical for engineering products. Moreover, the potential of a small-scale accelerator neutron source in performing Bragg edge imaging is shown. The results in this work along with our previous work (Bakhtiari *et al.*, 2023), in which a conceptual target was designed, could be steps towards developing the Bragg edge imaging technique in Korea using an electron-based neutron source (Lee *et al.*, 2021).

2. Theoretical concepts

The basic concept of Bragg edge imaging has been extensively discussed elsewhere (Sato *et al.*, 2011; Boin *et al.*, 2011; Santisteban *et al.*, 2001) and is briefly presented here for completeness.

It is well known that the intensity of neutrons passing through a sample is attenuated according to the Beer–Lambert–Bouguer law as follows:

$$\mathrm{Tr}(\lambda) = \frac{I(\lambda)}{I_0(\lambda)} = \exp\left[-\sigma_{\mathrm{tot}}(\lambda)\rho t\right], \qquad (1)$$

where $\mathrm{Tr}(\lambda)$ is the transmittance, λ is the neutron wavelength, I and I_0 are the transmitted and incident neutron-beam intensities, respectively, σ_{tot} is the neutron total cross section, ρ is the atomic number density, and t is the sample thickness.

The total cross section in equation (1) includes several components, namely coherent elastic scattering, incoherent elastic scattering, inelastic scattering and absorption cross sections (Ramić *et al.*, 2022; Sato *et al.*, 2011):

$$\sigma_{\mathrm{tot}}(\lambda) = \sigma_{\mathrm{ela}}^{\mathrm{coh}}(\lambda) + \sigma_{\mathrm{ela}}^{\mathrm{incoh}}(\lambda) + \sigma_{\mathrm{inela}}(\lambda) + \sigma_{\mathrm{abs}}(\lambda). \qquad (2)$$

The inelastic cross section has coherent and incoherent parts. However, in this work, we consider both as the inelastic cross section.

Each cross-section component reduces the neutron intensity in the transmission direction passing through the sample. Sudden discontinuities appear in the total cross section for polycrystalline materials, such as iron. Neutron coherent elastic scattering produces such sudden discontinuities, which are known as Bragg edges. These edges occur at a certain neutron wavelength, which corresponds to the {*hkl*} family of lattice planes of the crystal so that Bragg's law of $\lambda = 2d_{hkl}\sin\theta$ reads as $\lambda = 2d_{hkl}$, where d is the interplanar lattice spacing. Above this wavelength, the particular {*hkl*} no longer contributes to the neutron elastic scattering. The simplification of Bragg's law as $\lambda = 2d_{hkl}$ is due to the transmission geometry of the imaging setup and is not true in general. The cross sections for γ-Fe with face-centered cubic (f.c.c.) crystal structure [as evaluated by Ramić *et al.* (2022)] are shown in Fig. 1. The family of lattice planes for each Bragg edge is also shown in the figure. The coherent elastic cross section accounts for a major part of the total cross section for

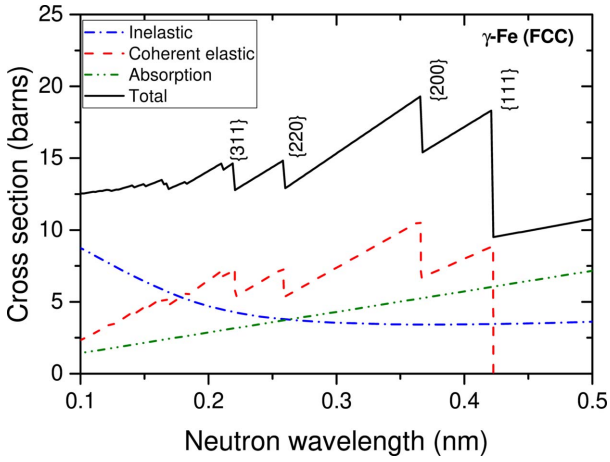

Figure 1
The inelastic, coherent elastic and total cross sections for γ-Fe (f.c.c.) obtained from Ramić *et al.* (2022). The absorption cross sections were obtained from the ENDF/B-VIII.0 library (Brown *et al.*, 2018). The family of lattice planes corresponding to each Bragg edge is indicated.

cold neutrons. The neutron absorption cross sections for Fe were taken from the ENDF/B-VIII.0 library (Brown *et al.*, 2018), and were added to the elastic and inelastic cross sections (Fig. 1).

In Bragg edge imaging, the crystallographic information of the polycrystalline material is extracted from the coherent cross section by fitting the measured neutron transmission spectra. In this work, the measured transmission spectra were analyzed using the *Rietveld Imaging of Transmission Spectra* (*RITS*) code (Sato *et al.*, 2011), which is discussed in Section 3.2.

3. Experimental procedure

3.1. Sample preparation

The AISI 304 stainless steel samples with nominal chemical composition that were used in this research are listed in Table 1. The samples were categorized in two different dimensions, as shown in Fig. 2. The first category included five samples with dimensions of $2.5 \times 2.5 \times 0.14$ cm^3 [Fig. 2(*a*)] and the second category had one $4 \times 4 \times 0.3$ cm^3 sample

Table 1
Nominal chemical composition of 304 austenitic stainless steel given in weight percentage (wt%).

Element	C	Si	Mn	Cr	Ni	N	Cu	Mo	Fe
wt%	0.05	0.40	1.10	17.0–19.0	7.0–10.0	0.04	0.27	0.086	Balance

[Fig. 2(*b*)]. The normal direction (ND), which is parallel to the neutron beam, rolling direction (RD) and transverse direction (TD) are also shown in the figure.

Each sample had a different characteristic to be measured via Bragg edge imaging. The samples shown in Fig. 2(*a*) comprised one CR with a reduction ratio of 60% and four heat-treated samples annealed at 950, 1080, 1160 and 1200°C for a time duration of 90 s. Full reversion occurs, in which martensite converts to austenite, after annealing of the CR sheet to 750°C. Different grain sizes can be obtained depending on the time and temperature of the annealing process due to recrystallization and grain growth (Kheiri *et al.*, 2019; Sun *et al.*, 2015). The heat treatment was performed in a laboratory-scale tube furnace, and after the annealing process, the samples were cleaned by immersing them into a hot acid pickling bath. The CR sample contained austenite (f.c.c.) and martensite (body-centered tetragonal, b.c.t.) phases. It is expected that the martensite phase would be removed by applying annealing (Hedayati *et al.*, 2010). Therefore, the annealed samples would be a single phase of austenite. The sample shown in Fig. 2(*b*) was produced via hot rolling of a thick plate to 3 mm thickness at 1080°C. The sample information is summarized in Table 2.

Two identical replicas for each sample shown in Fig. 2 were prepared. One set of these samples was used for the Bragg edge imaging experiment and the other for EBSD analysis. For the EBSD measurement, the samples were mechanically polished to 1200 SiC paper mesh size and electrochemically polished to remove the strain effect formed during the mechanical polishing. A LectroPol-5 electrolytic polishing instrument (Struers ApS, Ballerup, Denmark) was used to perform the electrochemical polishing under 22 V at room temperature. The electrolyte contained 20% perchloric acid and 80% ethanol.

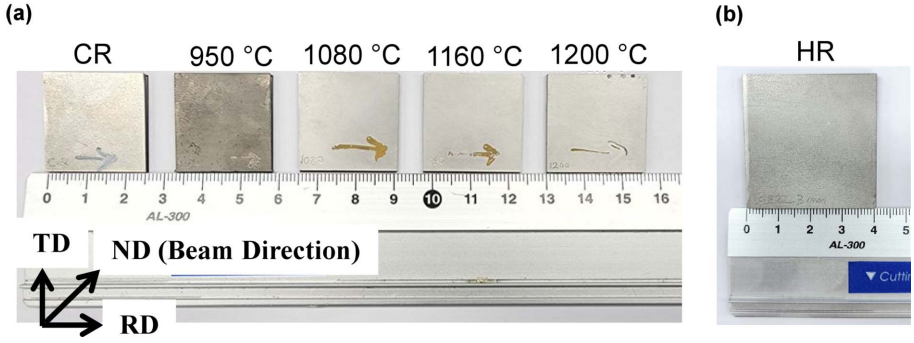

Figure 2
Photographs of the type 304 stainless steel samples. (*a*) CR sample (60% reduction ratio) and heat-treated samples at annealing temperatures of 950, 1080, 1160 and 1200°C with dimensions of $2.5 \times 2.5 \times 0.14$ cm^3. (*b*) HR sample at 1080°C with dimensions of $4 \times 4 \times 0.3$ cm^3.

Table 2
List of prepared samples for the Bragg edge imaging experiment performed at HUNS.

All the samples were irradiated simultaneously.

Sample	Condition		Dimension (cm^3)	Phase	Irradiation time (h)
CR	60% reduction ratio		2.5 × 2.5 × 0.14	Austenite and martensite	13.4
Annealed	Annealing temperature (°C)	Annealing time (s)			
	950	90	2.5 × 2.5 × 0.14	Austenite	13.4
	1080	90			
	1160	90			
	1200	90			
HR	–	–	4 × 4 × 0.3	Austenite	13.4

3.2. Bragg edge imaging measurement

The Bragg edges of the steel samples were measured using the neutron TOF-imaging method at HUNS (Sato *et al.*, 2018). The electron linac for neutron production was operated with an electron energy of 32.4 MeV, an electron pulse width of 4 µs, a pulse repetition rate of 70 Hz, a mean current of 70 µA and an electron-beam power of 2.3 kW. The neutrons were generated by irradiating a target with electrons. The target consisted of W (as radiator) and Pb (as neutron generator) with dimensions of 7.1 × 4 × 0.8 cm^3 and 7.1 × 4 × 3 cm^3, respectively. The neutron moderator was a decoupled/poisoned-type polyethylene at ambient temperature, providing a neutron-wavelength resolution of 0.5% at 0.4 nm at a distance of 6.24 m. The target and moderator were surrounded by a 50 × 50 × 50 cm^3 graphite reflector. A 3.65Qc super-mirror guide tube with a length of 3.83 m and cross-sectional size of 8 × 8 cm^2 was installed in the neutron beamline. The total neutron flight length for this experiment was 6.24 m, and the neutron TOF was used to calculate the wavelength using this flight path length. The neutron flux at the sample position was less than 10^4 neutrons cm^{-2} s^{-1}. The target geometry, neutron extraction beamline, guide tube, and sample and detector positions are schematically shown in Fig. 3.

The neutron TOF spectra were measured using a boron-based gas electron multiplier (GEM) type detector (Uno *et al.*, 2012) manufactured by Bee Beans Technologies Co. Ltd in Japan. The detection area of the GEM detector was 10 × 10 cm^2 (128 × 128 pixel) with a pixel size of 0.8 mm. The detector was flushed with Ar/CO_2 (70:30) gas with a flow rate of 90 cm^3 min^{-1} during the measurement. The applied high voltage to the detector was −3040 V. For each event, the position and time (X, Y, T) were recorded and the digitized data were transferred to a PC via Ethernet for further analysis. The neutron TOF bin size was set to 5 µs. For analyzing the neutron transmission spectra, however, the TOF bin size was merged to 50 µs, corresponding to a wavelength bin size of 3.2 × 10^{-3} nm, to improve the statistics in each time bin. The average neutron count rate for the open beam (no sample) was 5.4 × 10^4 counts s^{-1} recorded by the GEM detector. The exposure time for flat-field data acquisition (no sample in the neutron beam) was 10 h, whereas it was 13.4 h in the case of samples (Table 2). The samples were attached on the detector surface using an aluminium plate, as shown in Fig. 4.

In order to remove the background neutrons scattered from the samples, a grid collimator made of Gd_2O_3 with a thickness of 0.86 cm was placed in front of the GEM detector. The effect of background neutrons on transmission neutron spectra is discussed in detail by Sato *et al.* (2021). The neutron flight path length calibration and parameter determination of the Bragg edge profile function were carried out using a standard texture-free α-Fe sample (Sato *et al.*, 2021) with a thickness of 1 cm. These calibrated values were subsequently used in the *RITS* code for the fitting process.

The neutron-wavelength resolution obtained in this experiment was 0.5%, measured using the ⟨110⟩ Bragg edge of

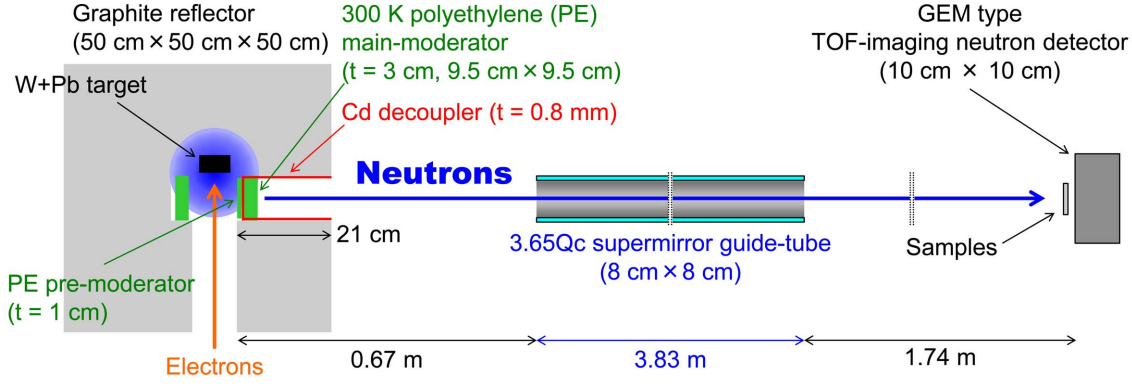

Figure 3
A schematic view of the neutron-generating target and the components of the Bragg edge imaging of HUNS. The dimensions are not to scale.

the standard texture-free α-Fe sample. This value is comparable to that of other large neutron sources. ISIS 'IMAT' provides a wavelength resolution of $\Delta\lambda/\lambda < 0.8\%$ for $\lambda > 2$ Å at a distance of 56 m and a spatial resolution better than 210 µm, depending on the field of view and detector type (Minniti *et al.*, 2018). J-PARC MLF BL22 'RADEN' has a wavelength resolution of $\Delta\lambda/\lambda > 0.2\%$ for $\lambda > 3$ Å at a distance of 23 m and a spatial resolution of larger than 100 µm for a counting-type detector, *e.g.* a GEM detector (Shinohara *et al.*, 2020). Although huge neutron sources provide far higher neutron intensities and a better spatial resolution than CANSs, performing experiments at such large neutron sources is very competitive due to the high demand for their beam time. Therefore, CANSs are a candidate to solve such limitations by providing reasonable wavelength and spatial resolutions, as will be discussed in Section 4.

The crystalline phase volume fraction, degree of crystallographic anisotropy and crystallite size can be quantitatively obtained using the *RITS* full pattern fitting using the Bragg edge of a specific {*hkl*} family of lattice planes. In the *RITS* code, the neutron transmission spectrum is fitted using a non-linear least-squares fitting algorithm based on a generalized form of the analytical expression of the coherent elastic cross section (Sato *et al.*, 2011) indicated in equation (2).

The crystallographic anisotropy is affected by the preferred orientation in a polycrystalline material and, consequently, the shape of the Bragg edges can significantly change (Sato *et al.*, 2011). The *RITS* code uses the March–Dollase (MD) (Larson & Von Dreele, 2004) preferred-orientation function for texture analysis. In the *RITS* analysis, a preferred orientation of $\langle hkl \rangle$ is assumed and the MD coefficient R is obtained. The value of the MD coefficient R is used to interpret the degree of crystallographic anisotropy. If R is equal to 1, the selected $\langle hkl \rangle$ vector has no preferred orientation and crystals have a random orientation distribution. Therefore, the sample does not present any texture. On the other hand, values of R smaller or larger than 1 indicate crystallographic anisotropy (texture), so for $R < 1$ and $R > 1$, the $\langle hkl \rangle$ preferred orientation is parallel and perpendicular to the neutron beam, respectively (Sato *et al.*, 2011). In this texture analysis, the neutron-beam direction is important as the reference direction to describe the preferred orientations of a family of lattice planes. For all the samples used in the neutron irradiation, the ND is parallel to the neutron-beam direction. The dependence of texture on the RD and the TD could not be distinguished. Therefore, hereafter, all results are described in terms of the neutron-beam direction.

Crystallite size determination in the *RITS* code is based on Sabine's primary extinction function (Sabine, 1985; Sato *et al.*, 2011). According to the extinction effect, neutron transmission increases as the crystallite size increases because neutrons are re-diffracted into the neutron transmission direction. A perfect crystal block or 'crystallite' is smaller than the grain and is equivalent to a sub-grain in a ductile metal (Sabine, 1985). The crystallite size of a sample is the average value along the sample thickness parallel to the neutron-beam direction.

In addition, the multiple crystalline phases are quantitatively evaluated by obtaining the projected atomic number density ρt (t = effective thickness) shown in equation (1) for each phase. The phase volume fraction is then estimated using the following equation (Su *et al.*, 2016; Sato *et al.*, 2021):

$$V_{\rm M} = \frac{\rho_{\rm M}(a_{\rm M}^3/2)}{\rho_{\rm M}(a_{\rm M}^3/2) + \rho_{\rm A}(a_{\rm A}^3/4)}, \tag{3}$$

where $\rho_{\rm M}$ and $\rho_{\rm A}$ are the projected atomic number densities and $a_{\rm M}$ and $a_{\rm A}$ are the lattice constants of martensite and austenite, respectively. The martensite phase has a b.c.t. crystal structure with a unit cell containing two atoms, while the austenite phase has an f.c.c. crystal structure with a unit cell containing four atoms.

In this work, first, the averaged spectrum over the whole area of each sample was fitted and analyzed using the *RITS* code, and the crystallographic data were extracted. Then the position-dependent TOF transmission spectrum was fitted for each pixel to obtain a two-dimensional distribution of the crystallographic quantities across the samples. The

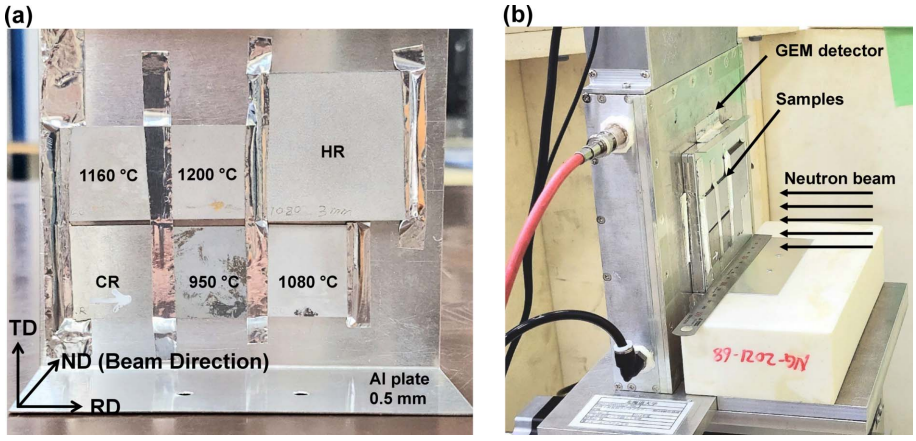

Figure 4
(*a*) A photograph of the six samples with their NDs parallel to the neutron beam attached onto an aluminium plate, ready to be irradiated simultaneously. (*b*) The samples placed in front of the GEM detector in the neutron beamline. The 0.86 cm-thick grid collimator (Gd_2O_3) is between the samples and the GEM detector.

transmission spectra were smoothed by moving an averaging filter of a 2 × 2 pixel area (1.6 × 1.6 mm^2) stepped at 1 pixel intervals. The TOF time channel was 50 µs.

The microstructure (crystallite size) and crystallite orientation (texture) of all the samples were measured using Bragg edge imaging. In the case of the CR sample, the phase volume fraction was also obtained. All the measured data were validated with EBSD as an established microscopy method in material characterization.

3.3. EBSD method

Field-emission scanning electron microscopy (JEOL model JSM-7900F operating at an accelerating voltage of 20 kV and 15 nA probe current) was used to characterize the samples before and after annealing. A scanning area of 350 × 400 µm^2 with a step size of 0.7 µm was used for the analysis. The local crystallographic orientation, grain size and phase discrimination of the samples were determined by EBSD analysis. The EBSD data were extracted using *Aztec* v6.1 (Oxford Instruments) and analyzed using *AztecCrystal* v2.0.

4. Results and discussion

4.1. Bragg edge imaging results

In this section, the results are discussed for the six samples; one CR, four annealed and one HR. The results are then compared with the EBSD data in Section 4.2. Radiographic images of the samples shown in Fig. 4 are given in Fig. 5. The HR sample attenuates neutrons more than the other samples and a higher signal-to-noise ratio could be obtained as its thickness is almost twice that of the other samples. Neutron transmission spectra integrated over the regions of interest (ROIs) marked with rectangular boxes for each sample are shown in Fig. 6(*a*) for a neutron wavelength between 0.1 and 0.5 nm. The Bragg edges of the HR sample are quite sharp and clearly seen even at lower neutron wavelengths. It is found

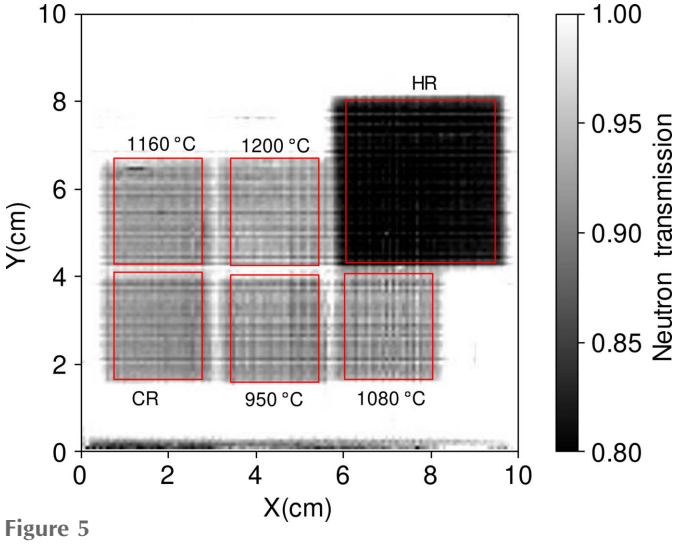

Figure 5
Radiographic images of the six samples shown in Fig. 2. The ROI for each sample is marked with a red rectangle. The area of the ROIs is 3.52 × 4 cm^2 for the HR sample and 2.0 × 2.48 cm^2 for the other samples.

that there is no preferred orientation of the crystallites and they are isotropic for the HR sample. For the other samples, the Bragg edges are affected by the crystallite size (extinction effect) and anisotropic orientations (texture) of crystallites. This conclusion will be investigated in more detail by Bragg edge imaging and EBSD analysis. First, the measured transmission spectra were integrated over the ROIs shown in Fig. 5 and were used in *RITS* analysis to obtain the average crystallographic information, and the fitting results are shown in Figs. 6(*b*)–6(*h*). Then, for reconstructing the two-dimensional distributions of the crystallite size, texture and phase volume fractions, the data in 2 × 2 pixel ROIs were integrated and analyzed by the *RITS* code.

The neutron transmission spectra shown in Fig. 6(*a*) were analyzed around the main Bragg edge regions, which are indicated by dashed-rectangle boxes, for each sample to obtain the crystallographic information. The neutron transmission spectra were fitted by means of the *RITS* code (Sato *et al.*, 2011) and the results are indicated in Figs. 6(*b*)–6(*h*). The crystallite size, MD coefficient *R* and projected atomic number densities were obtained and are listed in Table 3 along with their covariance values.

The CR sample with 60% reduction ratio included two phases of austenite (f.c.c.) and martensite (b.c.t.). Since the Bragg edge transmission spectrum of the b.c.t. phase is consistent with that of the body-centered cubic (b.c.c.) phase, a b.c.c. phase was assumed in this analysis. For the austenite phase, the double MD function (Sato *et al.*, 2021) was applied, and ⟨110⟩ and ⟨111⟩ were assumed as the preferred orientations in the *RITS* analysis, while for the b.c.c. phase, the single MD function with ⟨211⟩ as the preferred orientation was considered for the texture analysis. These orientation vectors were selected to attain the best fitting results. Since the double MD function was used in the *RITS* code, the weight of each preferred orientation was also obtained and is given in percentage in Table 3. As can be seen from Fig. 6(*b*), the Bragg edge corresponding to the {200} family of lattice planes of austenite phase is not present under this orientation due to the sample texture and probably because of martensite phase existence. The average crystallite size for the austenite and martensite phases was obtained as 0.2 and 2.3 µm, respectively. Therefore, the martensite phase has larger average crystallite size than the austenite phase. The MD coefficient *R* for the ⟨110⟩ and ⟨111⟩ orientations was obtained as 0.2 and 3.9, respectively, indicating that strong texture exists in this sample. The MD coefficient *R* for the ⟨211⟩ orientation was determined as 4.7, which shows that this orientation vector is perpendicular to the neutron-beam direction. The projected atomic number density, which is defined as ρt, for the austenite and martensite phases was found to be 0.71 × 10^{22} and 0.39 × 10^{22} cm^{-2}, respectively. The average austenite and martensite volume fractions over the entire measured region of the sample were calculated to be 64 and 36%, respectively, using equation (3).

In contrast to the CR sample, the Bragg edges corresponding to the {200} and {111} family of lattice planes are present for the 950°C sample. It seems that the martensite

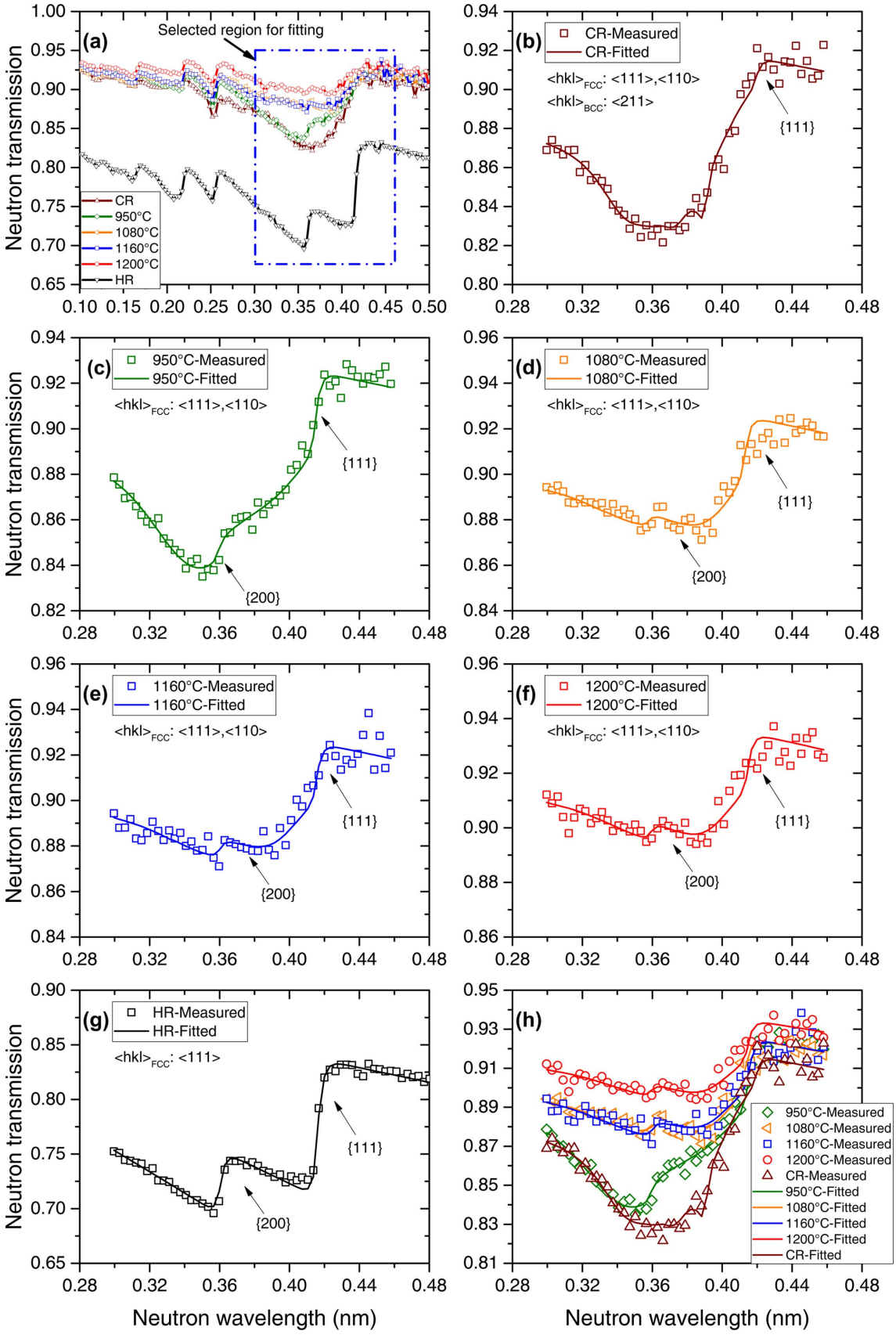

Figure 6
(*a*) Integrated neutron transmission spectra over the marked ROIs shown in Fig. 5 for each sample, and fitted results for (*b*) the CR sample composed of martensite and austenite phases, and for the (*c*) 950°C, (*d*) 1080°C, (*e*) 1160°C, (*f*) 1200°C and (*g*) HR samples. (*h*) The effect of crystallite size and texture on the Bragg edges for the CR and annealed samples. The assumed preferred orientations are shown for each transmission spectrum.

Table 3
Crystallite size, MD coefficient R and projected atomic number density with their covariance values for the CR, annealed and HR samples, obtained using the Bragg edge transmission measurement with *RITS* code analysis.

The weight of each orientation is given in parentheses.

Sample	Crystallite size (μm)	R: ⟨110⟩	R: ⟨111⟩	R: ⟨211⟩	ρt ($\times 10^{22}$ cm^{-2})
CR (f.c.c.)	0.2 ± 0.25	0.2 ± 0.02 (47%)	3.9 ± 0.19 (53%)	–	0.71 ± 0.05
CR (b.c.c.)	2.3 ± 0.2	–	–	4.7 ± 0.16 (100%)	0.39 ± 0.05
950°C	0.6 ± 0.14	0.3 ± 0.01 (77%)	2.9 ± 0.14 (23%)	–	0.99 ± 0.01
1080°C	4.2 ± 0.16	0.3 ± 0.02 (32%)	2.8 ± 0.16 (68%)	–	0.99 ± 0.01
1160°C	4.2 ± 0.17	0.4 ± 0.03 (68%)	3.4 ± 0.17 (32%)	–	0.99 ± 0.01
1200°C	4.9 ± 0.18	0.4 ± 0.04 (39%)	3.3 ± 0.16 (61%)	–	0.86 ± 0.01
HR	2.0 ± 0.16	–	1.0 ± 0.07 (100%)	–	2.26 ± 0.01

phase is removed by annealing the CR sample at 950°C, which allows the {200} Bragg edge to appear. The measured transmission spectrum for the ROI of 950°C shown in Fig. 5 was fitted very well and is depicted in Fig. 6(*c*). In the fitting, it was assumed that only the f.c.c. austenite phase was present, with the preferred orientations of ⟨110⟩ and ⟨111⟩. The crystallite size of the austenite was 0.6 μm, and the MD coefficient R was obtained as 0.3 and 2.9 for ⟨110⟩ and ⟨111⟩, respectively. Compared with the CR sample, the average crystallite size is slightly increased after the annealing process. However, the crystallite growth after recrystallization is not yet activated completely. In addition, this sample shows strong texture parallel to the beam for ⟨110⟩, and also strong texture perpendicular to the neutron beam for ⟨111⟩. The texture strength is slightly lower than that of the CR sample. The projected atomic number density for the austenite phase was obtained as 0.99×10^{22} cm^{-2}.

The neutron transmission spectra were also fitted for the samples annealed at 1080, 1160 and 1200°C, as indicated in Figs. 6(*d*), 6(*e*) and 6(*f*), respectively. The crystallite sizes were obtained as 4.2, 4.2 and 4.9 μm; the MD coefficients for the ⟨110⟩ orientation were derived as 0.3, 0.4 and 0.4; and those of the ⟨111⟩ orientation were extracted to be 2.8, 3.4 and 3.3, respectively. The average crystallite size grows as the annealing temperature increases. The projected atomic number densities for samples annealed at 1080 and 1160°C were both 0.99×10^{22} cm^{-2}, while that for 1200°C was 0.86×10^{22} cm^{-2}. This is interpreted as a reduction of the effective thickness.

The neutron transmission spectrum for the HR sample was also analyzed using the *RITS* code by assuming ⟨111⟩ for the preferred orientation, and a good fitting was obtained according to the reduced chi-squared value [Fig. 6(*g*)]. The crystallite size was obtained as 2.0 μm and the MD coefficient R was 1. For this sample, it can be concluded that there is no strong texture and that the crystallites have quite random orientations. The projected atomic number density was determined as 2.26×10^{22} cm^{-2}, which is larger than that of the other samples. This result was expected as the thickness of the HR sample is 0.3 cm and the other sample thicknesses are 0.14 cm.

The measured and fitted spectra for the CR and annealed samples are plotted together in Fig. 6(*h*) to show the neutron transmission spectrum and Bragg edge variations. The neutron transmittance increases from CR to 1200°C as the annealing temperature increases. This is because the austenite crystallites grow as the samples are annealed at the higher temperatures. On the other hand, the neutron transmittance increases as the crystallite size grows according to the extinction effect (Sabine, 1985), as mentioned before. The magnitude of the extinction effect is proportional to the size of the crystallites (DiJulio *et al.*, 2020). The extinction effect on the transmission spectra is clearly seen in our measured data. Furthermore, the transmission spectra are significantly affected for textured materials (Malamud *et al.*, 2014; Busi *et al.*, 2022) depending on the orientation of a specific {*hkl*} family of lattice planes. It is seen from Fig. 6(*h*) that the transmission spectra for the {111} family of lattice planes change due to the texture and crystallite size variations in each sample. Therefore, one can quickly obtain some qualitative insights about the microstructure and texture by examining the neutron transmission spectra.

4.2. Comparison with the EBSD method

The EBSD method was used to validate the measured microstructures and textures of the stainless steel samples

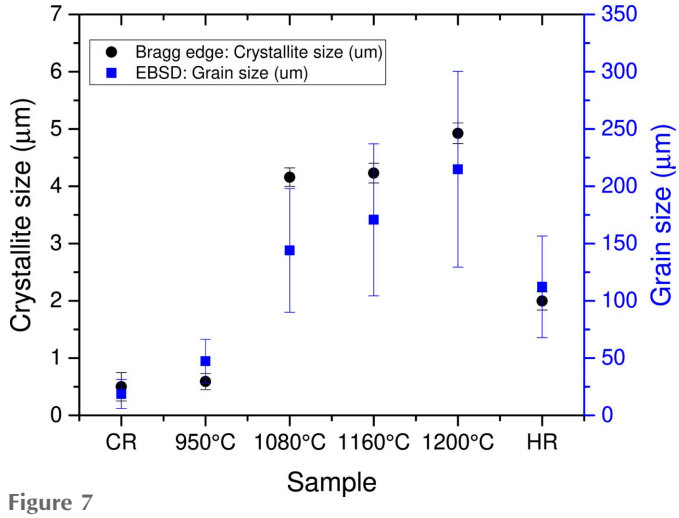

Figure 7
Weighted average crystallite size measured by Bragg edge imaging compared with the grain sizes obtained by EBSD for different type-304 stainless steel samples. The amount of martensite is negligible for the annealed and HR samples.

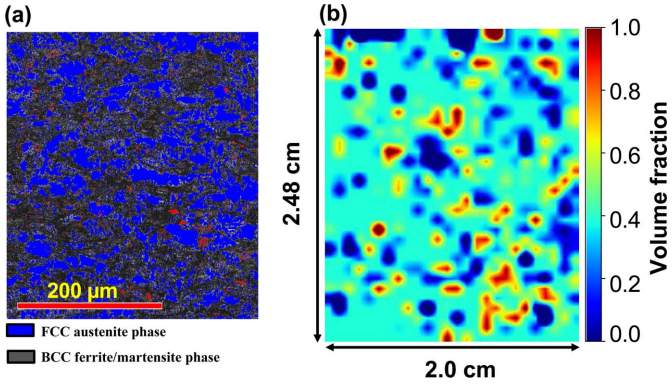

Figure 8
(*a*) Martensite and austenite phase distributions in the CR sample, measured by the EBSD method. (*b*) Phase volume fraction of martensite measured by Bragg edge imaging.

measured by Bragg edge imaging. The grain size, phase fraction and texture of the samples were analyzed.

The crystallite sizes obtained from Bragg edge imaging are plotted via the left axis of Fig. 7. The grain sizes obtained by EBSD were 18.7 ± 12.7, 47.3 ± 19.2, 144.0 ± 54.0, 170.7 ± 6.4, 214.9 ± 85.5 and 112.2 ± 44.4 µm for the CR, 950°C, 1080°C, 1160°C, 1200°C and HR samples, respectively, and are depicted in Fig. 7 via the right axis. A 10° misorientation was set as high-angle grain boundary criterion for EBSD, considering the annealing twin boundary as a high-angle boundary. The estimated crystallite size derived from the Bragg edge imaging in all samples is ∼50 times smaller on average than the grain sizes obtained by EBSD. The cause of the discrepancy is that the size of a crystallite indicates the area where the neutron beam generates diffraction due to the coherent elastic cross section. In contrast, the EBSD analysis carried out in this study offers information about the size of the austenite grain, which is constrained by the grain boundaries and probably made up of subgrains and stacking faults (Oba *et al.*, 2015; Su *et al.*, 2016). They both indicate a similar trend of crystallite/grain growth with the annealing temperature.

As was mentioned above, a martensite phase is induced during the cold-rolling process, and therefore the CR sample contains both austenite and martensite phases. The phase map obtained by EBSD is shown in Fig. 8(*a*). According to the EBSD analysis, the volume fraction of martensite phase was approximately 47% in the CR sample. These results indicate that the martensite phase volume fraction of 34% calculated by the Bragg edge imaging is reasonable. In addition, the martensite phase volume fraction within the bulk CR sample measured by the Bragg edge imaging is illustrated in Fig. 8(*b*). The martensite volume fraction of ∼50% is almost homogeneous over the sample, which is in agreement with the EBSD phase map. For the annealed samples, the EBSD measurement showed that all of the martensite phase was removed and only the austenite phase remained. However, the results are not shown here (Sadeghi *et al.*, 2021). The absence of the martensite phase could be explained by the neutron transmission spectra shown in Fig. 6 as the {200} family of lattice planes appeared in the annealed samples, indicating the reversion of martensite to austenite phase after heat treatment of the CR sample.

In addition, the quantitative two-dimensional distributions for crystallite size were analyzed using the *RITS* code for the ROIs shown in Fig. 5 by applying a 2×2 pixel averaging filter. For the CR sample, the crystallite size is given by a weighted average of martensite and austenite phases considering their volume fractions. It can be seen from Fig. 9(*a*) that the crystallite size grows from the CR sample to the 1200°C sample depending on the annealing temperature, and these results are in good qualitative agreement with the EBSD grain-size data

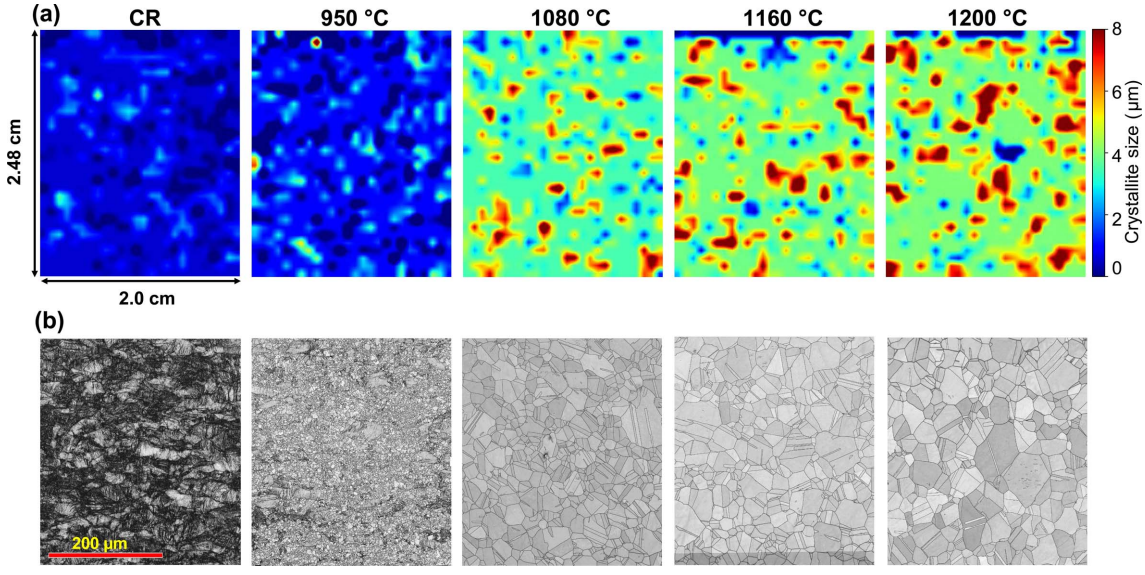

Figure 9
Comparison of crystallite/grain-size growth for the CR, 950, 1080, 1160 and 1200°C samples. (*a*) A quantitative illustration of crystallite size measured by Bragg edge transmission imaging and (*b*) grain-size growth measured by the EBSD method. The panels in (*a*) are the same size as the sample sizes, while the scale of the panels in (*b*) is in micrometres.

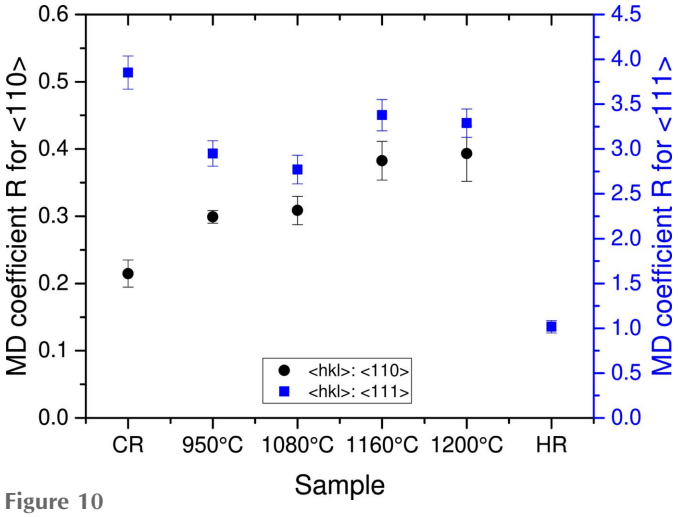

Figure 10
Variation of the MD coefficient R for the measured steel samples for ⟨110⟩ and ⟨111⟩ orientation directions. For the HR sample, only the ⟨111⟩ orientation was used.

shown in Fig. 9(*b*). The size of the images for the Bragg edge imaging are similar to the sample sizes, while the EBSD data are obtained by scanning a very small area with dimensions of 350 × 400 μm^2. This is an advantage of Bragg edge imaging to investigate the crystallographic information across a wide area of the bulk samples.

The MD coefficients R for ⟨110⟩ and ⟨111⟩ orientations extracted from the fitting are shown in Fig. 10. The results indicate that the MD coefficient R for ⟨110⟩ orientations steadily increases toward 1 from the CR sample to 1200°C. This means that the cold-rolling process causes strong texture in the ⟨110⟩ direction for this sample, while the annealing process reduces the texture, which might be due to the recrystallization. On the other hand, the MD coefficient R shows a different behavior for the ⟨111⟩ orientation. For the CR sample, R is far larger than 1, which indicates that the ⟨111⟩ orientation is perpendicular to the neutron beam (ND), while R reduces for the samples annealed at 950 and 1080°C. Therefore, the texture strength is reduced. In contrast, R increases again for the annealed samples at 1160 and 1200°C, indicating texture becoming stronger for this direction. For the HR sample, only ⟨111⟩ was assumed as the preferred orientation, and the corresponding MD coefficient R is shown in Fig. 10. Its value close to 1 means that no texture exists. These results are compared with the EBSD data and are discussed below.

A map of refined parameter R in the austenite steel for the CR and 950, 1080, 1160 and 1200°C samples is shown in Fig. 11(*a*) for the preferred orientation of ⟨110⟩. The coefficient R has small values in the CR sample and it gradually reaches values closer to 1. This means that the ⟨110⟩ orientation is largely parallel to the neutron beam (ND) in the CR sample, indicating strong texture in the sample. For the annealed samples, the texture gradually reduces and is quite weak at 1200°C as the blue regions appear.

In addition, the texture analysis obtained from the Bragg edge imaging is compared with the inverse pole figures (IPFs) obtained by EBSD and illustrated in Fig. 11(*b*). The IPFs are taken in the ND of the samples, showing which orientations are parallel to the neutron beam (ND). There is a strong texture for ⟨101⟩ for the CR sample and it gradually reduces for the annealed samples. The texture is quite relaxed for the 1200°C sample, indicating the same trend as for the Bragg edge imaging.

Fig. 12(*a*) shows a map of refined parameter R for the ⟨111⟩ orientation obtained by Bragg edge imaging and Fig. 12(*b*) shows EBSD IPFs taken in the RD (perpendicular to the neutron beam) for the CR and 950, 1080, 1160 and 1200°C samples. Many of the crystals have their ⟨111⟩ orientation

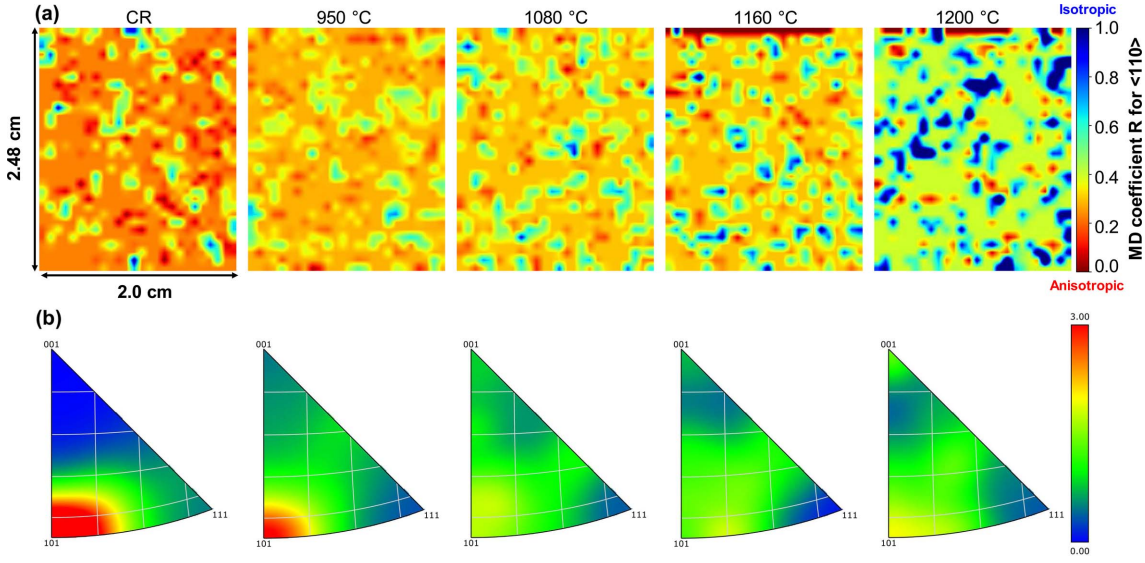

Figure 11
(*a*) Quantitative illustration of the degree of anisotropic crystallite orientation by MD coefficient R for the orientation vector ⟨110⟩, measured by Bragg edge transmission imaging, and (*b*) IPFs in the ND (parallel to the neutron-beam direction) obtained by the EBSD method, for the CR and 950, 1080, 1160 and 1200°C samples.

perpendicular to the neutron-beam direction for the CR sample ($R > 1$). On the other hand, the texture strength decreases in the 950 and 1080°C samples, and it again increases in the 1160 and 1200°C samples. The EBSD IPFs shown in Fig. 12(*b*) exhibit the same trend: a strong texture exists in the CR sample, then it reduces slightly in the 950 and 1080°C samples, and it increases for the 1160 and 1200°C samples. In this case, the EBSD data evidently confirm the Bragg edge imaging results as well.

A map of crystallite size for the HR sample is shown in Fig. 13(*a*). The average crystallite size is larger compared with the CR sample and the annealed sample at 950°C [Fig. 9(*a*)]. The phase-contrast map measured by EBSD is shown in Fig. 13(*b*) and also indicates grain growth due to the heating process. The texture variation across the HR sample measured by Bragg edge imaging is illustrated in Fig. 13(*c*) and it indicates that the MD coefficient R is around 1, which means a random distribution of crystals in the sample. The IPFs in the

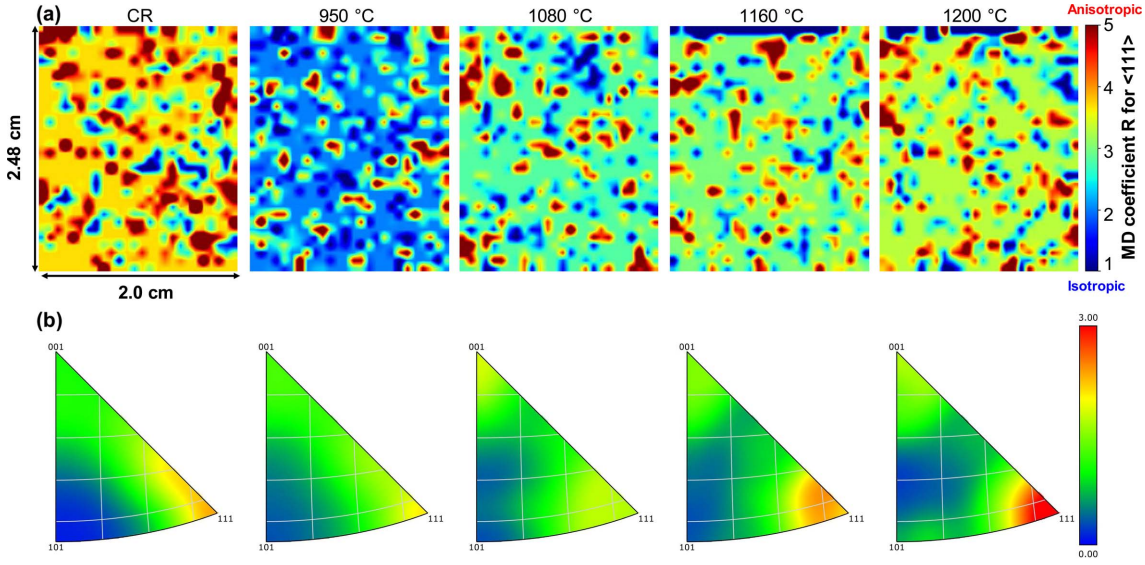

Figure 12
(*a*) Quantitative illustration of the degree of anisotropic crystallite orientation by MD coefficient R for the orientation vector ⟨111⟩, measured by Bragg edge transmission imaging, and (*b*) IPFs in the RD (perpendicular to the neutron-beam direction) obtained by the EBSD method, for the CR and 950, 1080, 1160 and 1200°C samples.

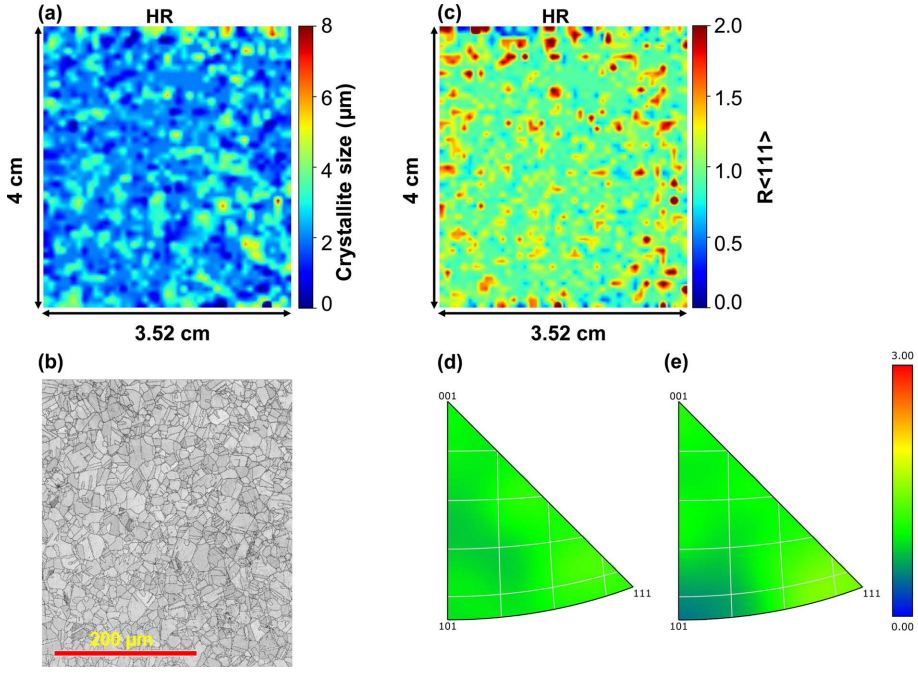

Figure 13
Two-dimensional maps of (*a*) crystallite size measured by Bragg edge imaging, (*b*) phase contrast by EBSD, (*c*) the MD coefficient R, (*d*) an EBSD IPF in the ND (parallel to the neutron-beam direction) and (*e*) an EBSD IPF in the RD (perpendicular to the neutron-beam direction), for the HR sample.

normal and rolling directions obtained by the EBSD method are shown in Figs. 13(*d*) and 13(*e*), indicating that almost no texture exists in the sample. The reason for randomly oriented crystals could be the recrystallization. The occurrence of recrystallization in deformed polycrystalline materials results in the formation of newly developed grains that exhibit either random orientation or weak texture (Humphreys & Hatherly, 2012; Ramadhan *et al.*, 2019).

5. Conclusions

TOF neutron Bragg edge imaging was performed at HUNS to study the microstructures and texture of type 304 stainless steel samples, which are important industrial products. Industrially produced steel sheets undergo several processes resulting in complex microstructure and texture, and are generally characterized by conventional methods such as EBSD and X-ray scattering. In this work, we successfully measured the crystallite size, texture and phase volume fraction of the bulk samples using Bragg edge imaging at a small-scale neutron source. The measured crystallographic information was validated by comparison with EBSD as the conventional method of material characterization, and a good qualitative agreement was obtained.

It was shown that the neutron transmission increased for the heat-treated samples as a function of the annealing temperature, as an indication of the crystallite size growth and the extinction effect. The Bragg edge results showed a similar trend to the EBSD analysis. The phase volume fraction of the CR sample was quantitatively determined and was reasonably consistent with the results obtained by EBSD. The texture evolution for the CR, HR and annealed samples was successfully evaluated by the Bragg edge imaging. The texture analysis of the Bragg edge imaging was performed with respect to the ND of the samples, which was parallel to the neutron-beam direction. The preferred orientation of ⟨110⟩ was strongly parallel to the neutron-beam direction for the CR sample and it gradually decreased as a result of the annealing process, showing less strong texture. The ⟨111⟩ orientation showed strong texture perpendicular to the neutron-beam direction for the CR sample. Its value slightly decreased for the samples heat treated at 950 and 1080°C and it again started to increase for those heat treated at 1160 and 1200°C. The EBSD measurement confirmed the texture evolution. The neutron transmission of the HR sample showed quite sharp Bragg edges, indicating a texture-free steel sample as the recrystallization causes randomly grown crystals.

The data presented in this work confirm that TOF neutron Bragg edge imaging is an effective and promising technique for studying the variation in texture and microstructures in actual engineering materials. Two-dimensional maps over a wide area of the samples were obtained without applying any destructive processes. Importantly, these data were obtained using a CANS and could be beneficial for developing a small-scale neutron source to be available for domestic and international users for material characterization.

Acknowledgements

The authors thank the students and staff of the Hokkaido University Neutron Source (HUNS) in Japan for their help and support during the experiment. We are also grateful to the Radiation Protection team at Pohang Accelerator Laboratory for their assistance with this research.

References

Albertini, G., Bruno, G., Fiori, F., Girardin, E., Giuliani, A., Quadrini, E. & Romani, F. (2000). *Physica B*, **276–278**, 925–926.
Anderson, I., Andreani, C., Carpenter, J., Festa, G., Gorini, G., Loong, C.-K. & Senesi, R. (2016). *Phys. Rep.* **654**, 1–58.
Bakhtiari, M., Jung, N.-S. & Lee, H.-S. (2022). *Nucl. Instrum. Methods Phys. Res. B*, **521**, 38–46.
Bakhtiari, M., Jung, N.-S., Um, W. & Lee, H.-S. (2023). *Nucl. Sci. Eng.* https://doi.org/10.1080/00295639.2022.2162791.
Boin, M., Hilger, A., Kardjilov, N., Zhang, S. Y., Oliver, E. C., James, J. A., Randau, C. & Wimpory, R. C. (2011). *J. Appl. Cryst.* **44**, 1040–1046.
Brown, D. A., Chadwick, M., Capote, R., Kahler, A., Trkov, A., Herman, M., Sonzogni, A., Danon, Y., Carlson, A., Dunn, M., Smith, D. L., Hale, G. M., Arbanas, G., Arcilla, R., Bates, C. R., Beck, B., Becker, B., Brown, F., Casperson, R. J., Conlin, J., Cullen, D. E., Descalle, M.-A., Firestone, R., Gaines, T., Guber, K. H., Hawari, A. I., Holmes, J., Johnson, T. D., Kawano, T., Kiedrowski, B. C., Koning, A. J., Kopecky, S., Leal, L., Lestone, J. P., Lubitz, C., Marquez Damian, J. I., Mattoon, C. M., McCutchan, E. A., Mughabghab, S., Navratil, P., Neudecker, D., Nobre, G. P. A., Noguere, G., Paris, M., Pigni, M. T., Plompen, A. J., Pritychenko, B., Pronyaev, V. G., Roubtsov, D., Rochman, D., Romano, P., Schillebeeckx, P., Simakov, S., Sin, M., Sirakov, I., Sleaford, B., Sobes, V., Soukhovitskii, E. S., Stetcu, I., Talou, P., Thompson, I., van der Marck, S., Welser-Sherrill, L., Wiarda, D., White, M., Wormald, J. L., Wright, R. Q., Zerkle, M., Zerovnik, G. & Zhu, Y. (2018). *Nucl. Data Sheets*, **148**, 1–142.
Busi, M., Polatidis, E., Malamud, F., Kockelmann, W., Morgano, M., Kaestner, A., Tremsin, A., Kalentics, N., Logé, R., Leinenbach, C., Shinohara, T. & Strobl, M. (2022). *Phys. Rev. Mater.* **6**, 053602.
Cho, S., Kim, J., Kim, T., Sato, H., Huh, I. & Cho, N. (2021). *Nucl. Eng. Technol.* **53**, 1619–1625.
Chowdhury, S. G., Das, S. & De, P. K. (2005). *Acta Mater.* **53**, 3951–3959.
DiJulio, D. D., Lee, Y. J. & Muhrer, G. (2020). *J. Neutron Res.* **22**, 275–279.
Donadille, C., Valle, R., Dervin, P. & Penelle, R. (1989). *Acta Metall.* **37**, 1547–1571.
Furusaka, M., Sato, H., Kamiyama, T., Ohnuma, M. & Kiyanagi, Y. (2014). *Phys. Procedia*, **60**, 167–174.
Hao, K., Gao, M. & Wu, R. (2020). *J. Mater. Res. Technol.* **9**, 124–132.
Hedayati, A., Najafizadeh, A., Kermanpur, A. & Forouzan, F. (2010). *J. Mater. Process. Technol.* **210**, 1017–1022.
Hendriks, J., Gregg, A., Jackson, R., Wensrich, C., Wills, A., Tremsin, A., Shinohara, T., Luzin, V. & Kirstein, O. (2019). *Phys. Rev. Mater.* **3**, 113803.
Hendriks, J. N., Gregg, A. W., Wensrich, C. M., Tremsin, A. S., Shinohara, T., Meylan, M., Kisi, E. H., Luzin, V. & Kirsten, O. (2017). *Phys. Rev. Mater.* **1**, 053802.
Huang, J.-x., Ye, X.-n. & Xu, Z. (2012). *J. Iron Steel Res. Int.* **19**, 59–63.
Humphreys, F. J. & Hatherly, M. (2012). *Recrystallization and Related Annealing Phenomena.* Oxford: Elsevier.
Kamiyama, T., Narita, Y., Sato, H., Ohnuma, M. & Kiyanagi, Y. (2017). *Phys. Procedia*, **88**, 27–33.
Kheiri, S., Mirzadeh, H. & Naghizadeh, M. (2019). *Mater. Sci. Eng. A*, **759**, 90–96.

Kino, K., Fujiwara, T., Furusaka, M., Hayashizaki, N., Kuroda, R., Michishio, K., Muroga, T., Ogawa, H., O'Rourke, B. E., Oshima, N., Satoh, D., Sei, N., Shishido, T., Suzuki, R., Tanaka, M., Toyokawa, H. & Watazu, A. (2019). *Nucl. Instrum. Methods Phys. Res. A*, **927**, 407–418.

Kockelmann, W., Minniti, T., Pooley, D. E., Burca, G., Ramadhan, R., Akeroyd, F. A., Howells, G. D., Moreton-Smith, C., Keymer, D. P., Kelleher, J., Kabra, S., Lee, T., Ziesche, R., Reid, A., Vitucci, G., Gorini, G., Micieli, D., Agostino, R., Formoso, V., Aliotta, F., Ponterio, R., Trusso, S., Salvato, G., Vasi, C., Grazzi, F., Watanabe, K., Lee, J., Tremsin, A., McPhate, J., Nixon, D., Draper, N., Halcrow, W. & Nightingale, J. (2018). *J. Imaging*, **4**, 47.

Larson, A. C. & Von Dreele, R. B. (2004). Report LAUR 86–748. Los Alamos National Laboratory, NM, USA.

Lee, C.-H., Moon, M., Lee, D. W., Kim, H. S., Kwon, H.-J., Lee, P., Kim, D. S., Seo, H. J., Hong, B. H., Lee, H.-S. & Bakhtiari, M. (2021). *J. Neutron Res.* **23**, 127–141.

Lu, L., Wang, X., Yang, Y. & Zhang, Z. (2020). *Nucl. Instrum. Methods Phys. Res. A*, **954**, 161793.

Malamud, F., Santisteban, J. R., Vicente Alvarez, M. A., Bolmaro, R., Kelleher, J., Kabra, S. & Kockelmann, W. (2014). *J. Appl. Cryst.* **47**, 1337–1354.

Minniti, T., Watanabe, K., Burca, G., Pooley, D. E. & Kockelmann, W. (2018). *Nucl. Instrum. Methods Phys. Res. A*, **888**, 184–195.

Naghizadeh, M. & Mirzadeh, H. (2016). *Metall. Mater. Trans. A*, **47**, 4210–4216.

Oba, Y., Morooka, S., Sato, H., Sato, N., Ohishi, K., Suzuki, J. & Sugiyama, M. (2015). *ISIJ Int.* **55**, 2618–2623.

Padilha, A. F., Plaut, R. L. & Rios, P. R. (2003). *ISIJ Int.* **43**, 135–143.

Raabe, D. (1997). *Acta Mater.* **45**, 1137–1151.

Ramadhan, R. S., Kockelmann, W., Minniti, T., Chen, B., Parfitt, D., Fitzpatrick, M. E. & Tremsin, A. S. (2019). *J. Appl. Cryst.* **52**, 351–368.

Ramadhan, R. S., Syed, A. K., Tremsin, A. S., Kockelmann, W., Dalgliesh, R., Chen, B., Parfitt, D. & Fitzpatrick, M. E. (2018). *Mater. Des.* **143**, 56–64.

Ramić, K., Marquez Damian, J. I., Kittelmann, T., Di Julio, D. D., Campi, D., Bernasconi, M., Gorini, G. & Santoro, V. (2022). *Nucl. Instrum. Methods Phys. Res. A*, **1027**, 166227.

Sabine, T. (1985). *Aust. J. Phys.* **38**, 507–518.

Sadeghi, F. (2022). PhD thesis, Pohang University of Science and Technology, Republic of Korea.

Sadeghi, F., Zargar, T., Kim, J. W., Heo, Y.-U., Lee, J. S. & Yim, C. H. (2021). *Materialia*, **20**, 101218.

Santisteban, J. R., Edwards, L., Steuwer, A. & Withers, P. J. (2001). *J. Appl. Cryst.* **34**, 289–297.

Sato, H., Kamiyama, T. & Kiyanagi, Y. (2011). *Mater. Trans.* **52**, 1294–1302.

Sato, H., Sasaki, T., Moriya, T., Ishikawa, H., Kamiyama, T. & Furusaka, M. (2018). *Physica B*, **551**, 452–459.

Sato, H., Sato, M., Su, Y., Shinohara, T. & Kamiyama, T. (2021). *ISIJ Int.* **61**, 1584–1593.

Sato, H., Watanabe, K., Kiyokawa, K., Kiyanagi, R., Hara, K., Kamiyama, T., Furusaka, M., Shinohara, T. & Kiyanagi, Y. (2017). *Phys. Procedia*, **88**, 322–330.

Shinohara, T., Kai, T., Oikawa, K., Nakatani, T., Segawa, M., Hiroi, K., Su, Y., Ooi, M., Harada, M., Iikura, H., Hayashida, H., Parker, J. D., Matsumoto, Y., Kamiyama, T., Sato, H. & Kiyanagi, Y. (2020). *Rev. Sci. Instrum.* **91**, 043302.

Shiota, Y., Hasemi, H. & Kiyanagi, Y. (2017). *Phys. Procedia*, **88**, 128–133.

Su, Y., Oikawa, K., Harjo, S., Shinohara, T., Kai, T., Harada, M., Hiroi, K., Zhang, S., Parker, J. D., Sato, H., Shiota, Y., Kiyanagi, Y. & Tomota, Y. (2016). *Mater. Sci. Eng. A*, **675**, 19–31.

Sun, G., Du, L., Hu, J., Xie, H., Wu, H. & Misra, R. (2015). *Mater. Charact.* **110**, 228–235.

Sun, G.-S., Hu, J., Zhang, B. & Du, L.-X. (2018). *Mater. Sci. Eng. A*, **732**, 350–358.

Tanhaei, S., Gheisari, K. & Alavi Zaree, S. (2018). *Int. J. Miner. Met. Mater.* **25**, 630–640.

Uno, S., Uchida, T., Sekimoto, M., Murakami, T., Miyama, K., Shoji, M., Nakano, E., Koike, T., Morita, K., Satoh, H., Kamiyama, & Kiyanagi, Y. (2012). *Phys. Procedia*, **26**, 142–152.

Vogel, S. (2000). PhD thesis, Christian-Albrechts Universität Kiel, Germany.